



# CHORUS

This is the accepted manuscript made available via CHORUS. The article has been published as:

## Autoionization resonances in the neon isoelectronic sequence using relativistic multichannel quantum-defect theory

M. Nrisimhamurty, G. Aravind, P. C. Deshmukh, and S. T. Manson

Phys. Rev. A **91**, 013404 — Published 8 January 2015

DOI: [10.1103/PhysRevA.91.013404](https://doi.org/10.1103/PhysRevA.91.013404)

# Autoionization resonances in neon isoelectronic sequence using relativistic multichannel quantum defect theory

Nrisimhamurty. Madugula<sup>†</sup>, G. Aravind<sup>†</sup>, P. C. Deshmukh<sup>†\*</sup>, and S. T. Manson<sup>‡</sup>

<sup>†</sup>Department of Physics, Indian Institute of Technology Madras, Chennai-600036, India\* and

<sup>‡</sup>Department of Physics and Astronomy,  
Georgia State University, Atlanta, GA 30303, USA

## Abstract

Studies of  $2s \rightarrow np$  autoionization resonances in the neon isoelectronic sequence using relativistic multichannel quantum defect theory (RMQDT) are reported. The relativistic random phase approximation (RRPA) is used to calculate the quantum defect parameters. The autoionization resonances are characterized using Fano resonance parameters. The results are compared with available experimental and theoretical data, and the behavior of the resonances as a function of  $Z$  is discussed.

PACS numbers: 32.80.Zb 32.80.Fb 32.80.Aa 32.80.Ee

---

\* pcd@physics.iitm.ac.in

## I. INTRODUCTION

Qualitative and quantitative knowledge of various observables resulting from the photoabsorption process is an important source of data for varied applications, such as modeling of the interstellar and intergalactic medium and development of x-ray free-electron lasers. The recent upsurge of interest in atomic photoabsorption [1–4] requires accurate atomic spectroscopic data. Quantum mechanical interference between bound  $\rightarrow$  continuum channels and bound  $\rightarrow$  bound channels lead to autoionization resonances [5–7]. Generally, autoionization is described as a two-step process that occurs when an excited atom/ion consisting of many electrons decays non-radiatively with the excited electron filling in a hole in a deeper bound state, enabling one of the other electrons bound with energy *less* than the excitation energy to escape into the unbound continuum. Autoionization is thus essentially a consequence of electron correlation and requires a many-body theory for its calculation. Studies of the autoionization resonances in the noble-gas atoms [5] have long attracted experimental and theoretical scrutiny. The significant cosmic abundance of neon-like highly charged ions (HCI), and the other similar atomic/ionic many-electron systems, has drawn special attention to their photoionization, with particular emphasis upon the asymmetric line profiles exhibited by the autoionization resonances [8–31]. Motivated by the astrophysical importance of HCIs, and by the anomalous behavior in Ne-like silicon and argon [21–23], the present work focuses primarily on the  $2s \rightarrow np$  autoionizing resonance transitions in the neon isoelectronic sequence.

The relativistic random phase approximation (RRPA) [32], which is a *whole-space* correlation theory, is employed to calculate the quantum defect parameters for the neutral neon atom and various ions isoelectronic with it. We then use the relativistic multichannel quantum defect theory (RMQDT) [33], a relativistic *partitioned-space correlation theory* based on Seaton’s formalism [34, 35] to study the autoionization resonances. The resonances are then characterized by their energies, widths and shape profiles in the form of the Fano parameters [4, 6].

## II. METHODOLOGY

The RRPA builds electron correlations by carrying out a linearization of the time-dependent Dirac-Hartree-Fock (DHF) formalism. Initial state correlations are included *via* the time-backward ring (and corresponding exchange) diagrams and the correlations in the final state are included *via* interchannel coupling corresponding to the time-forward ring (and corresponding exchange) diagrams. In the *full-RRPA*, all allowed relativistic dipole channels are coupled. However, in the present work, we have coupled only the important channels in *truncated-RRPA*. In particular, for the present study, we have included only interchannel coupling only between the following seven channels:

$$2p_{3/2} \rightarrow kd_{5/2}, kd_{3/2}, ks_{1/2}$$

$$2p_{1/2} \rightarrow kd_{3/2}, ks_{1/2}$$

$$2s_{1/2} \rightarrow kp_{3/2}, kp_{1/2},$$

where  $k = n$  for discrete in the case of the discrete bound  $\rightarrow$  bound channel and  $k = \epsilon$  for the bound  $\rightarrow$  continuum channels. In principle, the truncation causes loss of gauge invariance of the dipole matrix element resulting in a disagreement between length and velocity forms. Nevertheless, the disagreement between the two forms is rarely any worse than 5%, and usually much less since the  $1s$  photoionization channels are so far away energetically from the energy region of interest. Hence, in the present work, we have presented the results in the length form alone.

For linearly polarized incident light, the differential cross-section for an atomic subshell with quantum numbers  $n, \kappa$  is given by [32]:

$$\frac{d\sigma_{n\kappa}}{d\Omega} = \frac{\sigma_{n\kappa}(\omega)}{4\pi} [1 + \beta_{n\kappa}(\omega)P_2(\cos\theta)] \quad (1)$$

where  $\beta_{n\kappa}$  is the angular distribution asymmetry parameter,  $P_2$  is a Legendre polynomial,  $\theta$  is the angle between the photon polarization and the photoelectron momentum and  $\sigma_{n\kappa}$  is the total (angle integrated) cross-section for photoionization from the subshell  $(n\kappa)$ , and is written in terms of dipole matrix elements for the  $nj \rightarrow j'$  transitions as

$$\sigma_{n\kappa} = \frac{4\pi^2\alpha\omega}{3} (|D_{nj \rightarrow j-1}|^2 + |D_{nj \rightarrow j}|^2 + |D_{nj \rightarrow j+1}|^2), \quad (2)$$

with the matrix elements, calculated within the RRPA framework, given by

$$D_{nj \rightarrow \bar{j}} = i^{1-l} e^{i\delta_{\bar{\kappa}}} \langle \bar{\kappa} || \mathbf{Q}_1^{(1)} || \kappa \rangle_{RRPA} \quad (3)$$

in terms of the reduced matrix elements,  $\langle || \rangle$  and phase shifts,  $\delta_{\bar{k}}$ . The RMQDT parameters [33], such as the eigen-dipole amplitudes  $D_\alpha$ , eigen-quantum defects  $\mu_\alpha$  and the frame-transformation matrix elements,  $U_{i\alpha}$  depend only very weakly on the energy, thereby allowing interpolation of their values in the region of the autoionization resonances from values just outside this region calculated using RRPA. The autoionization resonances are then computed with RMQDT using these parameters. The values obtained using RRPA and RMQDT methodologies, which are reported here, have 5% uncertainty.

### III. RESULTS AND DISCUSSION

The DHF threshold energies used in these calculations for various ions and the neutral neon, along with other theoretical and experimental energies, are given in the Table I. Since electron correlations are not included in the DHF methodology, the DHF threshold energies are slightly higher than the experimental energies. Note, however, that it is not absolute energies we seek, but rather resonance energies with respect to the relevant thresholds; essentially quantum defects, and these will be seen to be much more accurate. However, to illustrate, the absolute energies are listed and compared with experiment and other calculations in Table I.

To set the stage for a discussion of the resonances, the RRPA non-resonant photoionization cross-sections, calculated including coupling among the 7 relativistic dipole channels described above, for atomic Ne,  $\text{Na}^+$ ,  $\text{Mg}^{2+}$ ,  $\text{Al}^{3+}$ ,  $\text{Si}^{4+}$  and  $\text{Ar}^{8+}$  above their respective  $2p_{1/2}$  thresholds are presented in Fig. 1(a). Note that the calculations have been carried out for a much larger set of ions, but only an illustrative subset is shown in detail. Note also that some of these cross-sections have been presented earlier [21] but are shown here for completeness. In any case, the cross-sections shown are the sum of the partial cross-sections from the  $2p_{3/2}$  and the  $2p_{1/2}$  subshells; the autoionizing region between the  $2p_{3/2}$  and the  $2p_{1/2}$  of each cross-section is omitted for clarity. The cross-section for neutral Ne shows a *delayed maximum* at about  $\sim 38$  eV, in agreement with earlier work [21, 41–44]; it occurs owing to the centrifugal potential barrier faced by the final state continuum d-waves, which overwhelms the attractive potential of the  $\text{Ne}^+$  ion. This *delayed maximum* appears even for the  $\text{Na}^+$  ion, but is not as pronounced as in the case of the neutral Ne atom, because of the stronger attractive nature of the  $\text{Ne}^{2+}$  ion in the final state. With increasing ionicity in the

Table I: Thresholds of outer subshells (eV).

Atom/ Ion	Thresholds of different subshells (eV)		
	2p <sub>3/2</sub>	2p <sub>1/2</sub>	2s
Ne	23.083 <sup>a</sup>	23.207 <sup>a</sup>	52.677 <sup>a</sup>
	21.566 <sup>b</sup>	21.663 <sup>b</sup>	48.475(E) <sup>e</sup>
	21.602 <sup>c</sup>	21.699 <sup>c</sup>	48.029(T) <sup>e</sup>
		21.661 <sup>d</sup>	
Na <sup>+</sup>	48.818 <sup>a</sup>	49.020 <sup>a</sup>	83.877 <sup>a</sup>
	47.287 <sup>b</sup>	47.465 <sup>b</sup>	80.073 <sup>f</sup>
	47.285 <sup>f</sup>	47.455 <sup>f</sup>	
Mg <sup>2+</sup>	81.682 <sup>a</sup>	81.998 <sup>a</sup>	122.356 <sup>a</sup>
	80.144 <sup>b</sup>	80.410 <sup>b</sup>	
Al <sup>3+</sup>	121.538 <sup>a</sup>	122.013 <sup>a</sup>	167.931 <sup>a</sup>
	119.9924(19) <sup>g</sup>	120.5249(19) <sup>g</sup>	167.0470(19) <sup>g</sup>
	119.9924(19) <sup>h</sup>	120.4192(19) <sup>h</sup>	164.4799(19) <sup>h</sup>
Si <sup>4+</sup>	168.318 <sup>a</sup>	169.01 <sup>a</sup>	220.526 <sup>a</sup>
	166.77 <sup>h</sup>	167.4 <sup>h</sup>	
	166.8(2) <sup>i</sup>	167.2(3) <sup>i</sup>	
	166.7 <sup>j</sup>	167.2 <sup>j</sup>	
P <sup>5+</sup>	221.987 <sup>a</sup>	222.962 <sup>a</sup>	280.106 <sup>a</sup>
Ar <sup>8+</sup>	424.142 <sup>a</sup>	426.51 <sup>a</sup>	500.675 <sup>a</sup>
	420.197 <sup>k</sup>	422.466 <sup>k</sup>	497.39 <sup>k</sup>
	422.54 <sup>h</sup> ; 422.20(12) <sup>l</sup> (2p thresholds)		497.44 <sup>h</sup>
	425.0 <sup>m</sup>	427.31 <sup>m</sup>	497.80(40) <sup>l</sup>
		501.92 <sup>m</sup>	
K <sup>9+</sup>	505.212 <sup>a</sup>	508.276 <sup>a</sup>	588.158 <sup>a</sup>
Ca <sup>10+</sup>	593.117 <sup>a</sup>	597.020 <sup>a</sup>	682.642 <sup>a</sup>
V <sup>13+</sup>	897.825 <sup>a</sup>	905.308 <sup>a</sup>	1008.297 <sup>a</sup>
Cr <sup>14+</sup>	1013.060 <sup>a</sup>	1022.162 <sup>a</sup>	1130.993 <sup>a</sup>
Fe <sup>16+</sup>	1264.041 <sup>a</sup>	1277.161 <sup>a</sup>	1397.766 <sup>a</sup>
	1262.7(7) <sup>h</sup>	1278.80 <sup>h</sup>	1394.71(7) <sup>h</sup>
	1265.8 <sup>m</sup>	1275.42(7) <sup>m</sup>	1399.31 <sup>m</sup>
Ni <sup>18+</sup>	1542.387 <sup>a</sup>	1560.743 <sup>a</sup>	1693.251 <sup>a</sup>
Ge <sup>22+</sup>	2181.300 <sup>a</sup>	2214.738 <sup>a</sup>	2371.491 <sup>a</sup>
Kr <sup>26+</sup>	2930.110 <sup>a</sup>	2986.607 <sup>a</sup>	3168.284 <sup>a</sup>
	2928.90(17) <sup>h</sup>	2984.25(17) <sup>h</sup>	
	2932.1 <sup>m</sup>	2988.36 <sup>m</sup>	3170.08 <sup>m</sup>
Zr <sup>30+</sup>	3789.213 <sup>a</sup>	3879.321 <sup>a</sup>	4086.719 <sup>a</sup>
Cd <sup>38+</sup>	5840.278 <sup>a</sup>	6041.968 <sup>a</sup>	6303.720 <sup>a</sup>
Xe <sup>44+</sup>	7672.183 <sup>a</sup>	8011.974 <sup>a</sup>	8317.617 <sup>a</sup>
	7660(4) <sup>h</sup>		
	7672.8 <sup>m</sup>	8011.98 <sup>m</sup>	8318.53 <sup>m</sup>
Nd <sup>50+</sup>	9758.418 <sup>a</sup>	10301.724 <sup>a</sup>	10654.559 <sup>a</sup>
Dy <sup>56+</sup>	12101.798 <sup>a</sup>	12935.758 <sup>a</sup>	13339.722 <sup>a</sup>
Ta <sup>63+</sup>	15165.047 <sup>a</sup>	16485.428 <sup>a</sup>	16954.945 <sup>a</sup>
Hg <sup>70+</sup>	18588.463 <sup>a</sup>	20609.196 <sup>a</sup>	21151.655 <sup>a</sup>
Bi <sup>73+</sup>	20167.490 <sup>a</sup>	22572.300 <sup>a</sup>	23148.485 <sup>a</sup>

<sup>a</sup>Present DHF thresholds, <sup>b</sup>Ref. [36] (E), <sup>c</sup>Ref. [16] (E), <sup>d</sup>Ref. [15] (E), <sup>e</sup>Ref. [37] (E), <sup>f</sup>Ref. [38]

(T), <sup>g</sup>Ref. [31] (T) <sup>h</sup>NIST [39, 40], <sup>i</sup>Ref. [22] (E), <sup>j</sup>Ref. [21] (E), <sup>k</sup>Ref. [25] (T), <sup>l</sup>Ref. [23] (E),

<sup>m</sup>Ref. [29] (T)(DARC results)

isoelectronic sequence, this *delay* disappears, as expected, since the ionic potential becomes strong enough to pull the continuum d-wave in, even at threshold. In  $\text{Si}^{4+}$ , the cross-section however increases rapidly from threshold from near zero and then decreases; this is due to a  $2s \rightarrow 3p$  resonance just at threshold which was discussed (and corroborated experimentally) earlier [21]. And, by  $\text{Ar}^{8+}$ , the hint of an increase in the cross-section at threshold is not the remnants of the shape resonance, but rather the effect of the nearby  $2s \rightarrow 4p$  resonance that lies slightly below threshold.

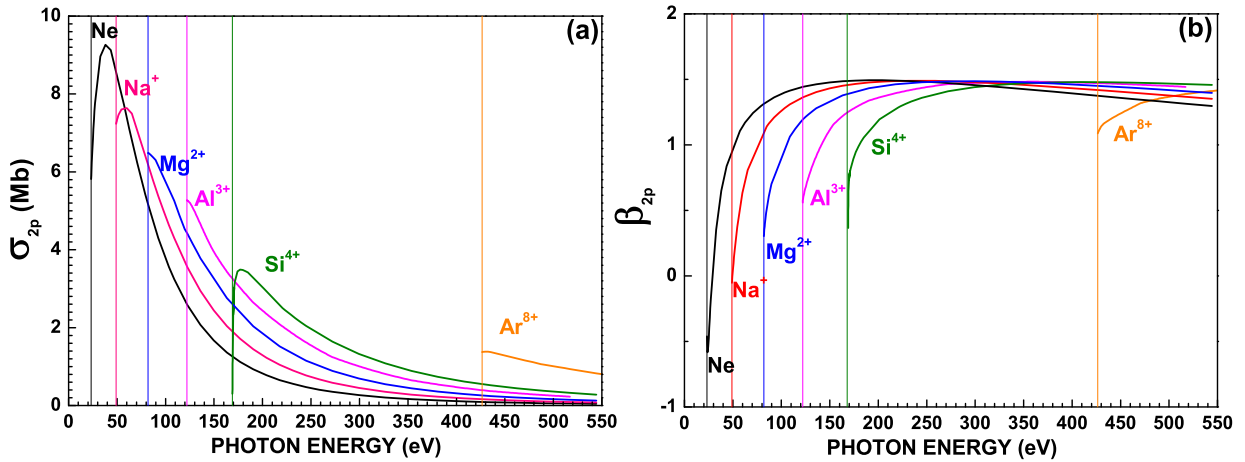


Figure 1: (a) Total 2p ( $2p_{3/2} + 2p_{1/2}$ ) non-resonant (background) photoionization cross-section for Ne,  $\text{Na}^+$ ,  $\text{Mg}^{2+}$ ,  $\text{Al}^{3+}$ ,  $\text{Si}^{4+}$  and  $\text{Ar}^{8+}$ ; (b) Weighted average (as described in the text) of the associated  $2p_{3/2}$  and  $2p_{1/2}$  photoelectron angular distribution asymmetry parameter. The vertical lines represent the respective ionization thresholds.

Also shown [in Fig. 1(b)] are the angular distribution asymmetry parameters,  $\beta$ , as a function of photon energy as a weighted (by respective partial cross-sections) average of the angular distribution asymmetry parameter for the  $2p_{3/2}$  and the  $2p_{1/2}$  subshells. The evolution of the  $\beta$ , as a function of  $Z$ , is clearly seen; they become flatter and flatter, as a function of energy, as the shape resonance moves further and further below threshold, except for the anomaly at  $\text{Si}^{4+}$  owing to the Feshbach resonance just at threshold. For neutral Ne, these results have been previously shown to be in excellent agreement with experiment [45]. Thus, it is rather likely that the calculations for the rest of the sequence are quantitatively accurate as well. This is of interest since the recent advent of UV and x-ray laser sources have made it possible to measure photoelectron angular distributions resulting from ionic photoionization; there are essentially no extant measurements of photoelectron

angular distributions resulting from ionic photoionization.

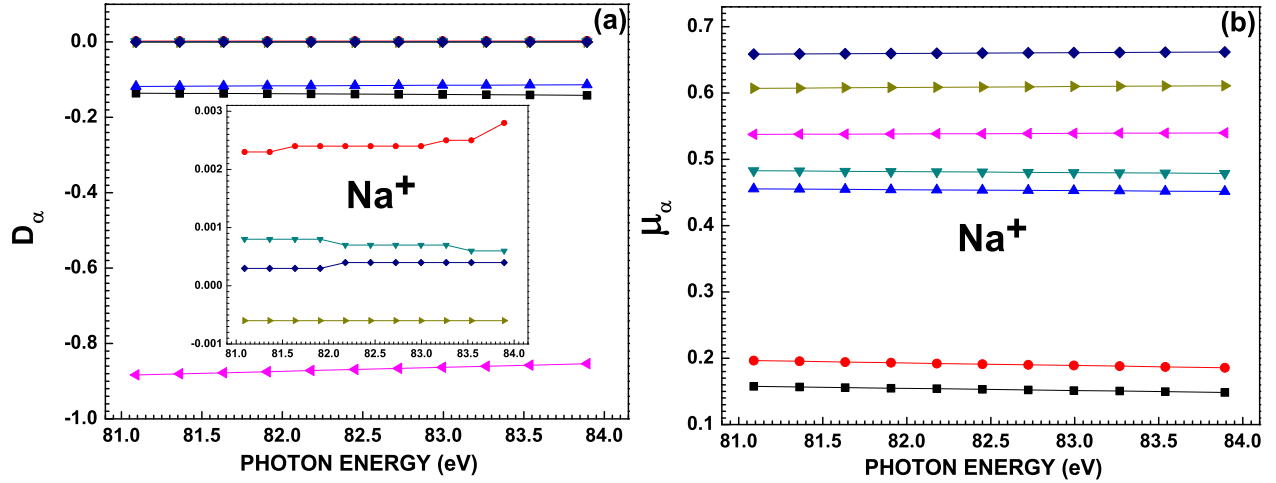


Figure 2: (a) Variation of eigen-amplitudes ( $D_\alpha$ ) and (b) eigen-quantum defects ( $\mu_\alpha$ ) of  $\text{Na}^+$  respectively as a function of photon energy (eV).

Turning our attention to the  $2s \rightarrow np$  resonances, it is crucial to note that, in general, MQDT parameters are almost insensitive to energy in the threshold region. As an example, for  $\text{Na}^+$ , we present in Fig. 2(a), the eigen-amplitudes ( $D_\alpha$ ), and in Fig. 2(b), the corresponding quantum defects ( $\mu_\alpha$ ) for the seven  $\alpha$ -channels arising from the  $2s$ ,  $2p_{1/2}$  and  $2p_{3/2}$  subshells of  $\text{Na}^+$  to illustrate the near-insensitivity to energy of the MQDT parameters obtained from the application of RRPA. Results of other members of the Ne isoelectronic sequence studied are qualitatively similar. The  $D_\alpha$  data for  $\text{Na}^+$  show that the channels  $n = 1, 3$  and  $5$ , the optically-allowed (mostly) singlet channels, are relatively stronger than the remaining four triplet channels and are possible at all results from the relativistic interactions.

Using RRPA to calculate the RMQDT parameters, and the latter to obtain the physical observables, the  $2s \rightarrow np$  autoionization resonances in the  $2p$  cross-section and corresponding angular distribution asymmetry parameter  $\beta$  have been obtained. To give some idea of how the spectrum changes along the sequence, the results for Ne,  $\text{Na}^+$ ,  $\text{Si}^{4+}$  and  $\text{Ar}^{8+}$  are presented in Figures 3 to 6, respectively. In each of these figures, (a), (b), (c) and (d) provide respectively the cross-section as a function of effective quantum number, the cross-section as a function of the photon energy,  $\beta$  as a function of the effective quantum number, and  $\beta$  as a function of the photon energy.

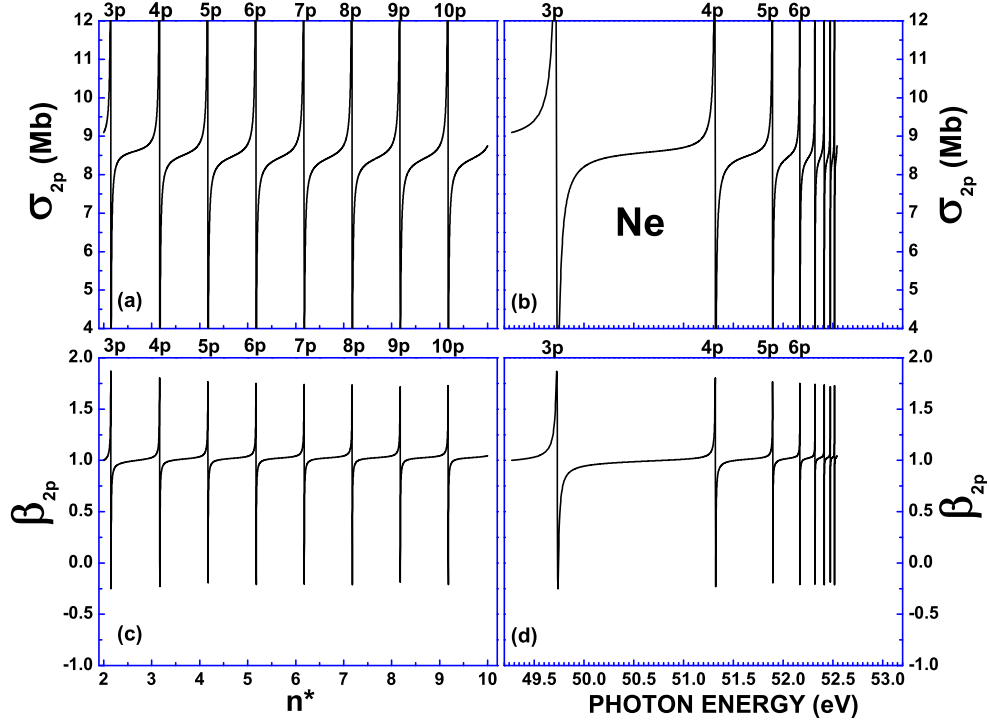


Figure 3: Total 2p cross-sections and (weighted average) angular distribution asymmetry parameters for Ne in the region of the  $2s \rightarrow np$  resonances shown vs, effective quantum number,  $n^*$ , and photon energy. The resonances are labelled.

The autoionization resonances in the 2p cross-section shown in Figures 3 to 6 are seen to be periodic functions of the effective quantum number  $n^*$ ; when plotted against energy they converge to their respective 2s thresholds. The quantum defects determined for Ne and for a few members of the isoelectronic ions are given in Table II, along with results using other theoretical methods and/or experimental techniques is presented. It is seen from this table that the present results are in quite good agreement with experimental and theoretical values reported in literature. For example, the quantum defect for the  $^1P$  resonance in atomic neon found from this work is about 0.84, which is in close agreement with the available theory (0.842) and experiment (0.832(6)) [19]. The background cross-section is about 8.8 Mb, in good agreement with the available experimental and theoretical data [19, 45]. The background value of the  $\beta$  parameter for Ne, as seen from Fig. 3, is roughly unity in this energy range. Based upon the general expression for  $\beta$ , this value is indicative of the  $p \rightarrow d$  matrix element being much larger than the  $p \rightarrow s$  channel [50–52]. This is one illustration of the detailed physics of the particular photoionization process that

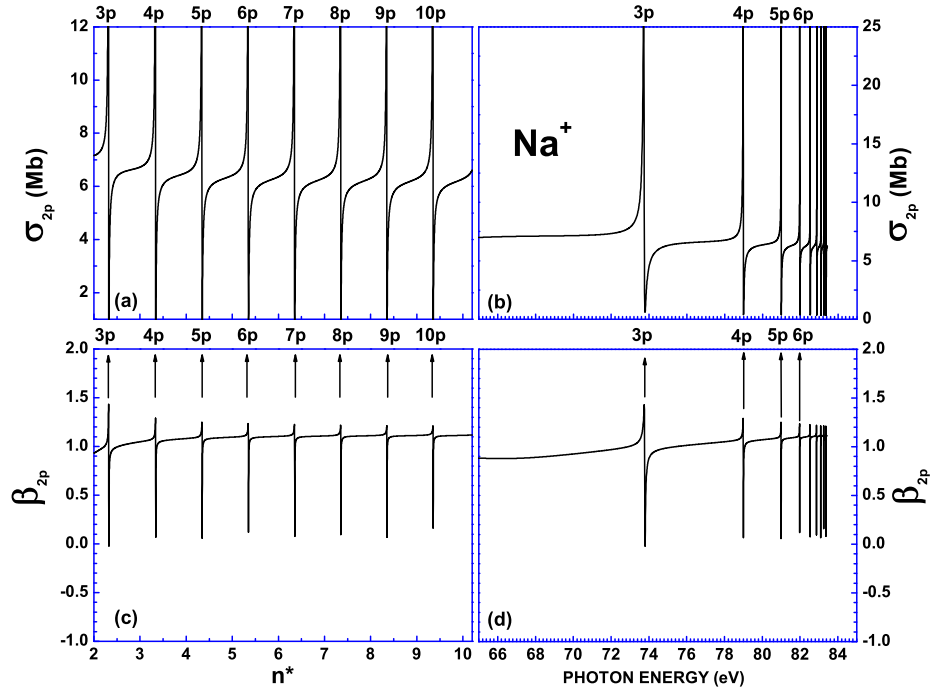


Figure 4: Total 2p cross-sections and (weighted average) angular distribution asymmetry parameters for  $\text{Na}^+$  in the region of the  $2s \rightarrow np$  resonances shown vs, effective quantum number,  $n^*$ , and photon energy. The resonances are labelled.

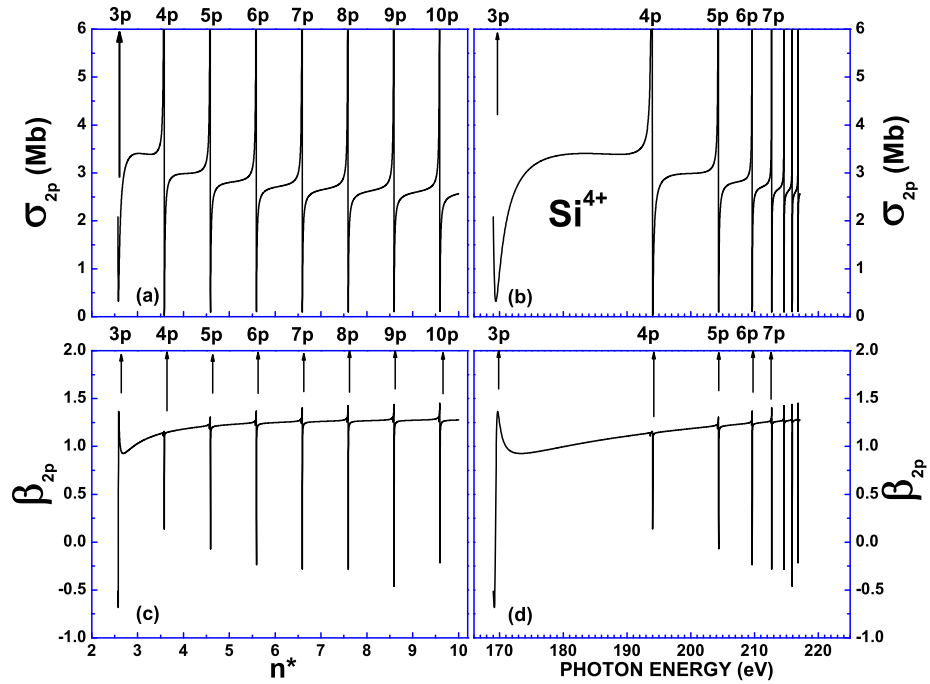


Figure 5: Total 2p cross-sections and (weighted average) angular distribution asymmetry parameters for  $\text{Si}^{4+}$  in the region of the  $2s \rightarrow np$  resonances shown vs, effective quantum number,  $n^*$ , and photon energy. The resonances are labelled.

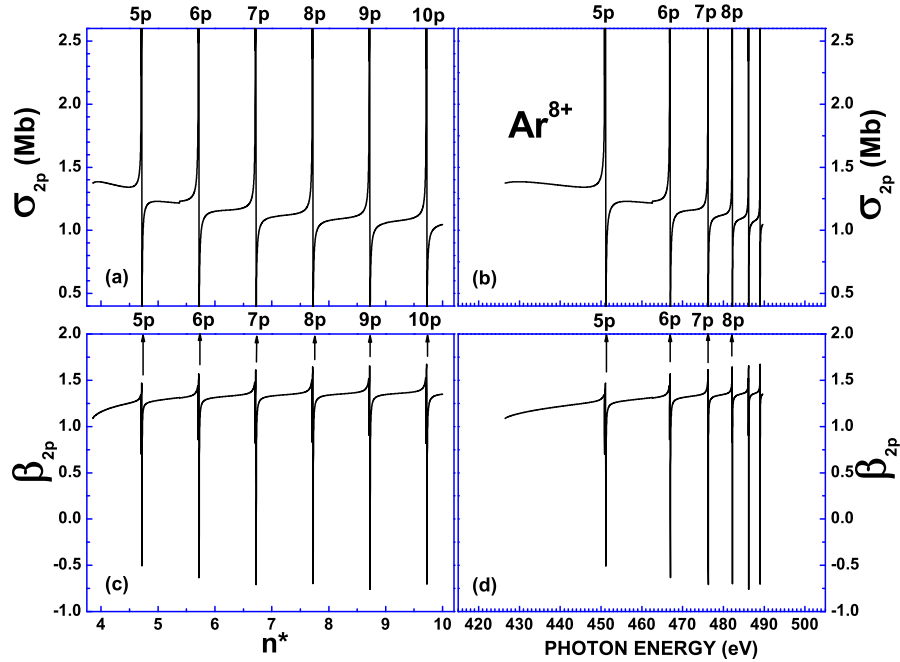


Figure 6: Total 2p cross-sections and (weighted average) angular distribution asymmetry parameters for  $\text{Ar}^{8+}$  in the region of the  $2s \rightarrow np$  resonances shown vs, effective quantum number,  $n^*$ , and photon energy. The resonances are labelled.

can be gleaned from studies of the photoelectron angular distribution, information which cannot be obtained from the cross-section itself.

For  $\text{Na}^+$  [Fig. 4], the background cross-section, in the resonance range, is somewhat smaller than that of Ne, and is decreasing over the range, from about 7.5 Mb to roughly 6 Mb. The resonance shapes differ somewhat as well. The background value of the  $\beta$  parameter is still unity, indicating that, in this case too, the  $p \rightarrow d$  transition dominates in this region. For  $\text{Al}^{3+}$ , the background cross-section is about 5.27 Mb above  $2p_{1/2}$  threshold and it gradually decreases to about 3.57 Mb, in the vicinity of  $2s$  threshold. The cross-section values for  $\text{Al}^{3+}$  are in close agreement with the reported values [30, 31]. The shapes of the resonances in the angular distribution parameter show marked differences from the Ne case. These trends are continued in  $\text{Si}^{4+}$  [Fig. 5] where the background cross-section varies from about 3.5 Mb to about 2.5 Mb over the resonance range and the resonance shapes are starting to differ markedly. The background  $\beta$  is seen to rise significantly above the value of unity, thus indicating that the  $p \rightarrow d$  channel is not so dominant in this case. Finally, for  $\text{Ar}^{8+}$  [Fig. 6], the background cross-section is significantly smaller, decreasing

Table II: Quantum defects  $\mu_{np}$  for the  $2s \rightarrow np$   $^1P$  resonances of the Ne isoelectronic sequence. The present work gives the asymptotic value calculated, while the experimental and previous theory give the range reported.

Atom/ion	Present work	Experiment	Previous theory
Ne	$\sim 0.84$	$\sim 0.832(6)^a$ $\sim 0.829-0.89^b$ $\sim 0.85-0.88^d$	$\sim 0.842^a$ $\sim 0.79-0.81^c$
Na <sup>+</sup>	$\sim 0.66$	$\sim 0.68-0.78^d$	
Mg <sup>2+</sup>	$\sim 0.55$	$\sim 0.57^d$	$\sim 0.31-0.6^e$ $\sim 0.48-0.56^f$
Al <sup>3+</sup>	$\sim 0.48$	$\sim 0.497^d(^1P_1)$	$\sim 0.44755-0.48047^g$
Si <sup>4+</sup>	$\sim 0.43$		
Ar <sup>8+</sup>	$\sim 0.28$	$\sim 0.286-0.33^h$	$\sim 0.27-0.28^i$ $\sim 0.27889^j(^1P_1)$
Fe <sup>16+</sup>	$\sim 0.17$		$\sim 0.17562^j(^1P_1)$
Kr <sup>26+</sup>	$\sim 0.116$		$\sim 0.12524^j(^1P_1)$
Xe <sup>44+</sup>	$\sim 0.074$		$\sim 0.09489^j(^1P_1)$

<sup>a</sup>Ref. [19], <sup>b</sup>Ref. [16], <sup>c</sup>Ref. [46], <sup>d</sup>Ref. [11], <sup>e</sup>Ref. [47], <sup>f</sup>Ref. [48], <sup>g</sup>Ref. [49], <sup>h</sup>Ref. [23], <sup>i</sup>Ref. [25]

<sup>j</sup>Ref. [29]

from 1.4 Mb to 1.1 Mb over the range, and the background value of  $\beta$  is as large as 1.4, thereby showing the decreasing dominance of the  $p \rightarrow d$  channel with increasing  $Z$  along the isoelectronic sequence.

Concerning quantum defects, it is known that, in the limit of infinite  $Z$ , all quantum defects approach zero because inter-electron interactions become irrelevant compared to the interaction with the nuclear charge in that limit. It is of interest, however, to investigate the detailed behavior of the quantum defects as a function of  $Z$  along an isoelectronic sequence. At low  $Z$ , which is governed by nonrelativistic physics, the quantum defect of a resonance is simply  $n - n^*$ , where  $n$  is the principal quantum number and  $n^*$  is the effective quantum number. But at higher  $Z$ , where relativistic physics and  $jj$  coupling hold sway, the relationship is not so simple; in that case, the quantum defect is given by [33, 35, 53]

$$\mu_{nlj} = n - n^* + (j + 1) - [(j + 1)^2 - (z\alpha)^2]^{1/2}, \quad (4)$$

where  $z$  is the asymptotic charge seen by the photoelectron, and  $\alpha$  is the fine-structure constant. Our RRPA results show that the lowest values of  $Z$  (or  $z$ ), the  $2s \rightarrow np$  transitions,

which result in final states  $2s2p^6np$ , are LS coupled,  $^1P_1$  or  $^3P_1$ , with the amplitude of the latter extremely small. But with increasing  $Z$ , the coupling rapidly moves away from LS and towards jj coupling and by  $Z=40$ , the final states are fully jj coupled,  $2s_{1/2}2p^6np_{1/2}$  and  $2s_{1/2}2p^6np_{3/2}$ , both coupled to  $J=1$ ; this is required for dipole transitions from a  $J=0$  initial state.

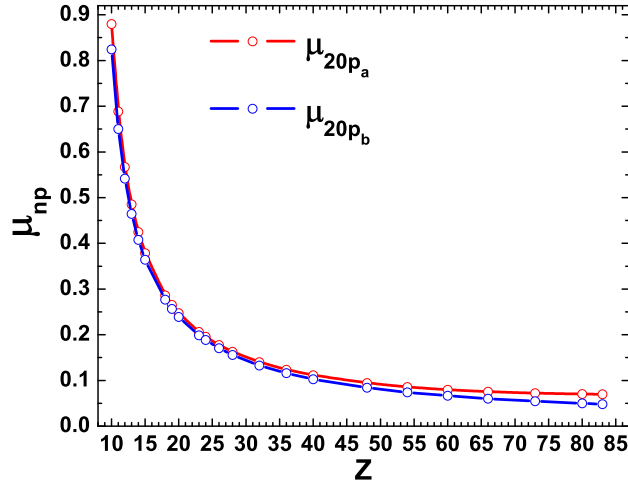


Figure 7: Quantum defects of the Ne isoelectronic sequence as functions of nuclear charge,  $Z$ . For low  $Z$ , the upper and lower curves represent the  $^3P$  and  $^1P$  resonances respectively, while for high  $Z$ , they represent the  $p_{1/2}$  and  $p_{3/2}$  excitations respectively.

The calculated asymptotic quantum defects (actually calculated for  $n = 20$ ) over the whole isoelectronic sequence are shown in Fig. 7, where the approach to zero, at the higher  $Z$  values, is evident. It is also clear that, as relativistic effects become important, the  $np$  quantum defects depend upon  $j$  and the  $p_{3/2}$  quantum defects approach zero more quickly than the  $p_{1/2}$ . This occurs because the  $np_{1/2}$  electrons are more compact than their  $np_{3/2}$  counterparts so more of their density is in the interior non-Coulomb region of the potential, which is where the quantum defect is generated. In the low- $Z$  region, the upper curve (larger quantum defects) represent the  $^3P$  resonances which are more tightly bound than the  $^1P$  owing to the fact that exchange interaction is attractive in the triplet case, and repulsive in the singlet states.

A recent theoretical study of Ne-like  $Cu^{19+}$  found the asymptotic quantum defects to be about 0.28 [54], in considerable disagreement from the present results of about 0.18, as seen in Fig. 7. Now, it can be shown on general grounds that the asymptotic quantum defects must decrease with increasing  $Z$ . However, as seen in Table II, the asymptotic quantum

defect for  $\text{Ar}^{8+}$  is about 0.28, and this is corroborated by an independent calculation [25]. Thus, it appears likely that the results of Ref. [54] are quantitatively in error. Settling this question is of astrophysical importance.

To compare theoretical cross sections with existing experimental data, we have applied a Gaussian convolution to our results for the autoionization resonance profiles with appropriate widths to simulate the measurements. In addition, the theoretical results have been shifted in energy to align the 2s thresholds with experiment by the amounts indicated in Table I. To give some idea of the effect(s) of the convolutions, in Fig. 8 are shown the convoluted theoretical 2s $\rightarrow$ np resonances in atomic neon along with the unconvoluted. The comparison shows clearly that the convoluted resonances are wider and of smaller amplitude than their unconvoluted counterparts; these *must* go together since the convolution preserves oscillator strength. The convolution does not affect the position of the resonances, nor does it affect the background cross-section. All the experimental results are of relative cross-section, so they were put on an absolute scale by normalizing experiment to theory in the region of the non-resonant continuum where the theoretical results are likely to be excellent. Using this procedure for the experimental cross-sections, the 2s $\rightarrow$ 3p, 2s $\rightarrow$ 4p and 2s $\rightarrow$ 5p resonances in neon atom, convoluted at 18 meV Full-width-at-half-maximum (FWHM), as quoted in Ref. [55], are shown in Fig. 9, along with the experimental data. From the comparison, it is evident that there is excellent quantitative agreement between theory and experiment for the 4p and 5p resonances. The agreement is seen to be less good for the 3p resonance. This is most probably due to the fact that the quantum defect parameters experience their greatest variation with energy, in this energy region, so that the interpolation required by the RMQDT methodology is mostly at risk here. However, as indicated earlier, the accuracy will improve with increasing Z, i.e., the situation for the Ne 2s $\rightarrow$ 3p resonance is the worst-case scenario.

Although there exists data for  $\text{Na}^+$  [20], it is not in a form that could be digitized and compared with herein. But there is accessible experimental data for  $\text{Ar}^{8+}$ , specifically in the region of the 2s $\rightarrow$ 5p resonance [23], which is the lowest resonance in the continuum for  $\text{Ar}^{8+}$ ; the 2s $\rightarrow$ 4p resonance is just below threshold, as discussed earlier, and the 2s $\rightarrow$ 3p resonance is well below threshold. A comparison with our calculated data is given in Fig. 10 where it is clear that agreement is quite good, despite the rather significant scatter in the experimental points. The results are in good agreement with the experiment when convoluted with a

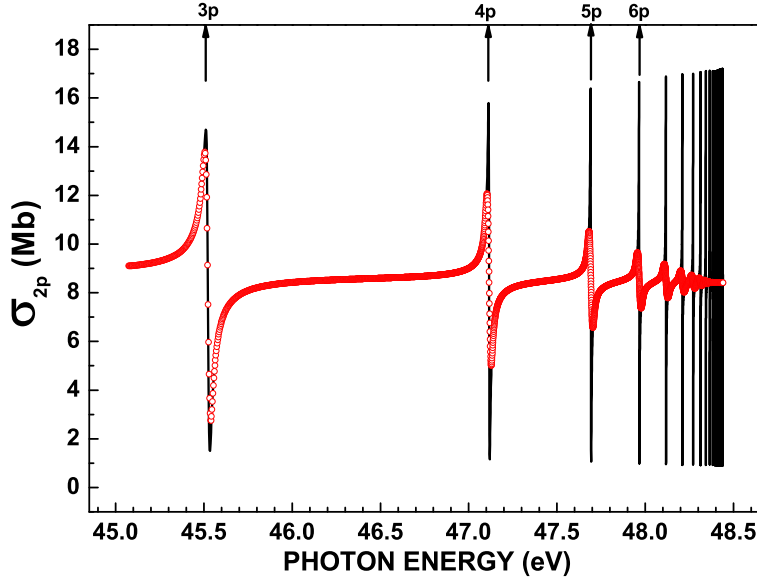


Figure 8: Total 2p photoionization cross-section in the region of the  $2s \rightarrow np$  resonances in atomic Ne obtained using RMQDT (solid line) and the cross section convoluted with  $\text{FWHM} = 18 \text{ meV}$  (open circles).

gaussian of FWHM of 100 meV. Based upon these comparisons with experiment then, we can be reasonably confident that the predictions of the present calculations should be reasonably accurate for the  $2s \rightarrow np$  resonances over the entire isoelectronic sequence above the lowest member of the series, in each case.

Now resonances can be characterized by parameters which are determined by their position, width and shape known as Fano parameters [6, 7, 16]. Using these parameters, the photoionization cross-section in a resonance region is given by

$$\sigma(E) = \sigma_0(E) \left[ (1 - \rho^2) + \rho^2 \left( \frac{(q + \epsilon)^2}{(1 + \epsilon^2)} \right) \right], \quad (5)$$

with  $\epsilon = \frac{(E - E_r)}{(\Gamma/2)}$ ,  $E_r$  being the resonance energy,  $\Gamma$  is the width,  $q$  is the shape parameter,  $\rho^2$  is the correlation coefficient and  $\sigma_0(E)$  is the background cross-section; the detailed cross-section in a resonance region can be specified completely using these parameters.

Our calculated Fano parameters are presented in Table III for cases where there is experimental data; specifically for Ne  $2s \rightarrow 3p$ ,  $2s \rightarrow 4p$ ,  $2s \rightarrow 5p$  and  $2s \rightarrow 6p$ ,  $2s \rightarrow 3p$  in  $\text{Na}^+$  and  $\text{Mg}^{2+}$  and for the  $2s \rightarrow 5p$  transition in  $\text{Ar}^{8+}$ . The table shows relatively good agreement between the present results and experiment in all cases shown, except for the  $2s \rightarrow 5p$  transition in  $\text{Ar}^{8+}$ . First of all, there is a non-negligible relativistic splitting between the two 5p

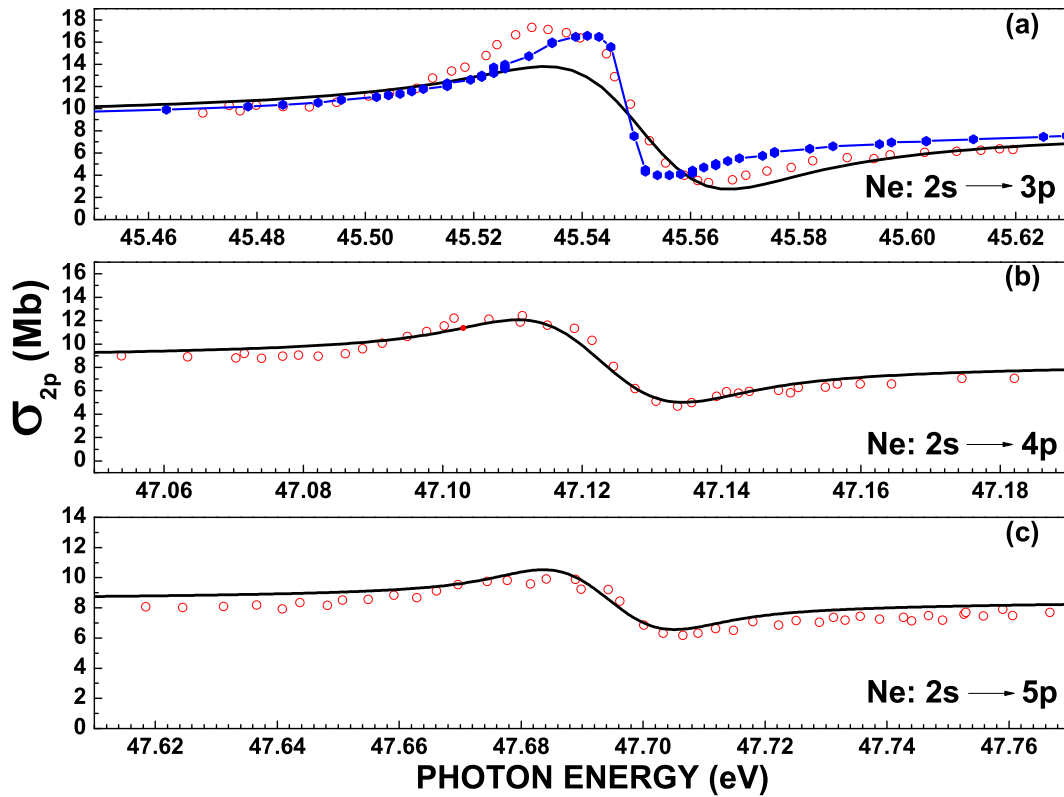


Figure 9: Total 2p cross section for Ne, convoluted at FWHM = 18 meV, in the region of the (a) 2s→3p, (b) 2s→4p, and (c) 2s→5p resonances (solid lines). Also shown are the experimental results of Ref. [55] (open circles) and Ref. [19] (connected solid diamonds).

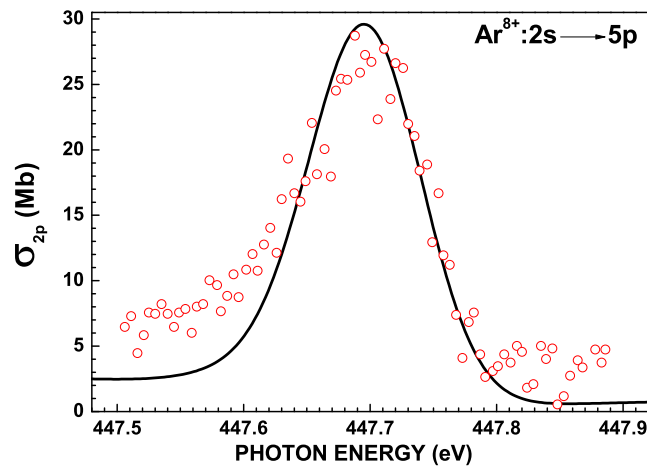


Figure 10: Total calculated 2p cross-section in the neighbourhood of the 2s→5p autoionization resonance in  $\text{Ar}^{8+}$ , convoluted with a 100 meV FWHM instrumental width (solid line) along with the experimental results of Ref.[23] (open circles).

Table III: Fano parameters for various resonances compared to experiment and previous theory. Experimental results are italicized. Uncertainties (where quoted) are given in parentheses.

Atom/ion: Resonance	Resonance Energy, $E_r$ (eV)	Width, $\Gamma$ (meV)*	Shape Parameter, q	Correlation Coefficient, $\rho^2$
Ne: $2s \rightarrow 3p$ Ne ( $2s2p^63p$ )	49.725 <sup>a</sup>	13 <sup>a</sup>	-1.4 <sup>a</sup>	0.77 <sup>a</sup>
	<i>45.5442</i> <sup>b</sup>	<i>16(2)</i> <sup>b</sup>	<i>-1.58(1)</i> <sup>c</sup>	<i>0.75(5)</i> <sup>c</sup>
	45.53397 <sup>b</sup>	34.9 <sup>b</sup>	-1.59(1) <sup>c</sup>	0.72 <sup>c</sup>
	45.557 <sup>c</sup>	<i>13.2(10)</i> <sup>c</sup>	<i>-1.53(1)</i> <sup>c</sup>	<i>0.73</i> <sup>c</sup>
	<i>45.546(8)</i> <sup>d</sup>	18.6(10) <sup>c</sup>	<i>-1.6(2)</i> <sup>d</sup>	<i>0.70(7)</i> <sup>d</sup>
	46.253 <sup>e</sup>	<i>13(2)</i> <sup>d</sup>	-3.69 <sup>e</sup>	0.514 <sup>e</sup>
	45.5655 <sup>f</sup>	13.9 <sup>e</sup>	-0.34 <sup>g</sup>	0.93 <sup>g</sup>
	45.538 <sup>h</sup>	11.4 <sup>f</sup>	-1.16 <sup>g</sup>	0.91 <sup>g</sup>
		11.7 <sup>g</sup>	-1.6 <sup>g</sup>	0.76 <sup>g</sup>
	12.1 <sup>g</sup>	-1.3 <sup>g</sup>	0.77 <sup>g</sup>	
	31.8 <sup>h</sup>	-1.32 <sup>h</sup>		
Ne: $2s \rightarrow 4p$ Ne ( $2s2p^64p$ )	51.318 <sup>a</sup>	7 <sup>a</sup>	-1.35 <sup>a</sup>	0.63 <sup>a</sup>
	<i>47.1193(50)</i> <sup>b</sup>	6.65 <sup>b</sup>	<i>-1.47(1)</i> <sup>c</sup>	<i>0.78(11)</i> <sup>c</sup>
	47.11092 <sup>b</sup>	<i>5.7(10)</i> <sup>c</sup>	-1.88 <sup>c</sup>	0.72 <sup>c</sup>
	47.111 <sup>c</sup>	4.3 <sup>c</sup>	-1.82 <sup>c</sup>	0.73 <sup>c</sup>
	<i>47.121(5)</i> <sup>d</sup>	<i>4.5(1.5)</i> <sup>d</sup>	<i>-1.6(3)</i> <sup>d</sup>	<i>0.70(7)</i> <sup>d</sup>
	47.397 <sup>e</sup>	3.86 <sup>e</sup>	-3.95 <sup>e</sup>	0.505 <sup>e</sup>
	47.1278 <sup>f</sup>	5.28 <sup>f</sup>	-1.75 <sup>g</sup>	0.76 <sup>g</sup>
	3.8 <sup>g</sup>	-1.46 <sup>g</sup>	0.77 <sup>g</sup>	
Ne: $2s \rightarrow 5p$ Ne ( $2s2p^65p$ )	51.894 <sup>a</sup>	3 <sup>a</sup>	-1.15 <sup>a</sup>	0.71 <sup>a</sup>
	<i>47.6952(15)</i> <sup>b</sup>	2.47 <sup>b</sup>	<i>-1.46(5)</i> <sup>c</sup>	<i>0.6(2)</i> <sup>c</sup>
	47.69182 <sup>b</sup>	<i>3.6(18)</i> <sup>c</sup>	-1.9 <sup>c</sup>	0.74 <sup>c</sup>
	47.687 <sup>c</sup>	1.8 <sup>c</sup>	-1.87 <sup>c</sup>	0.75 <sup>c</sup>
	<i>47.692(5)</i> <sup>d</sup>	<i>2(1)</i> <sup>d</sup>	<i>-1.6(5)</i> <sup>d</sup>	<i>0.70(14)</i> <sup>d</sup>
	47.814 <sup>e</sup>	1.62 <sup>e</sup>	-4.05 <sup>e</sup>	0.502 <sup>e</sup>
47.6975 <sup>f</sup>	2.61 <sup>f</sup>			
Ne: $2s \rightarrow 6p$ Ne ( $2s2p^66p$ )	52.168 <sup>a</sup>	1.58 <sup>a</sup>	-1.04 <sup>a</sup>	0.89 <sup>a</sup>
	<i>47.9650(30)</i> <sup>b</sup>	1.28 <sup>b</sup>		
	47.96708 <sup>b</sup>	1.44 <sup>f</sup>		
	47.9690 <sup>f</sup>			
Na <sup>+</sup> : $2s \rightarrow 3p$ Na <sup>+</sup> ( $2s2p^63p$ )	73.746 <sup>a</sup>	60 <sup>a</sup>	-1.8 <sup>a</sup>	0.9 <sup>a</sup>
	<i>69.95</i> <sup>i</sup>			
Mg <sup>2+</sup> : $2s \rightarrow 3p$ Mg <sup>2+</sup> ( $2s2p^63p$ )	101.525 <sup>a</sup>	90 <sup>a</sup>	-2.3 <sup>a</sup>	0.975 <sup>a</sup>
	98.2 <sup>j</sup>			
	<i>98.22</i> <sup>k</sup>			
Ar <sup>8+</sup> : $2s \rightarrow 5p$ Ar <sup>8+</sup> ( $2s2p^65p$ )	451.123 <sup>a</sup>	22.395 <sup>a</sup>	-7.6 <sup>a</sup>	0.866 <sup>a</sup>
	<i>447.71(10)</i> <sup>l</sup>	<i>30(5)</i> <sup>l</sup>	<i>-6(1)</i> <sup>l</sup>	
	447.54(30) <sup>l</sup>	29.01 <sup>m</sup>		
	447.726 <sup>m</sup>	25.8 <sup>n</sup>		
	447.33 <sup>n</sup>			

<sup>a</sup>Present results (RRPA+RMQDT, L form), <sup>b</sup>Ref. [19], <sup>c</sup>Ref. [55], <sup>d</sup>Ref. [16], <sup>e</sup>Ref. [56], <sup>f</sup>Ref.

[46], <sup>g</sup>Ref. [43], <sup>h</sup>Ref. [57], <sup>i</sup>Ref. [58], <sup>j</sup>Ref. [47], <sup>k</sup>Ref. [11], <sup>l</sup>Ref. [23], <sup>m</sup>Ref. [25], <sup>n</sup>Ref. [29]

resonances; however, owing to experimental instrumental width, and the fact that one 5p resonance is much weaker than the other, this does not show up experimentally, as seen in Fig. 10. Secondly, as discussed previously, the lowest member of each series is not quite so accurate with RMQDT, and this case is the lowest member of the resonance series for  $\text{Ar}^{8+}$ . Third, and most important, a very fine energy mesh is required to properly characterize a resonance. In this case, the experimental energy mesh was 5 meV [23]. On the theoretical side, Ref. [25] used 0.001 Ryd (13.6 meV), Ref. [59] used a mesh of about 0.0015 Ryd (about 20 meV), and  $\Delta n^* = 0.001$  (24.2 meV) [present work], in this energy region. We studied how different energy meshes will yield different cross-section profiles for  $\text{Ar}^{8+}$ , with  $\Delta n^* = 0.0001$  (2.42 meV),  $\Delta n^* = 0.001$  (24.2 meV) and  $\Delta n^* = 0.005$  (121 meV). We find that wider meshes yield more erroneous values and further scrutiny of these resonances, both theoretical and experimental, is warranted. However the oscillator strength of these resonances are preserved since the mesh splitting employed in the present work is smaller than the instrumental width.

In any case, it is well-known from quantum defect theory [34, 35] that the widths,  $\Gamma$ , of the higher Rydberg states decrease as  $(n^*)^3$  so that the product  $(n^*)^3\Gamma$  approaches a constant as  $n$  gets large. Thus, a knowledge of this constant for any given case, along with the asymptotic quantum defect, allows one to obtain the width of any state in the Rydberg series, except perhaps the lowest few. It is also of interest as to how this constant varies over the isoelectronic sequence. To investigate this, calculations have been performed for the  $n=20$  states of various members of the isoelectronic sequence and the widths obtained. As mentioned previously the two resonances for each  $n$  in the Ne isoelectronic sequence are essentially LS at low  $Z$  and jj at high  $Z$ , and some mixture and intermediate  $Z$  values. Thus the  $(n^*)^3\Gamma$  values for the two resonances for the ions in the Ne isoelectronic sequence are studied in the present work by labeling them as  $p_a$  and  $p_b$  resonances, and not as ‘singlet/triplet’ nor as ‘ $p_{1/2}/p_{3/2}$ ’.

The results of the calculations are shown in Table IV and Fig. 11. Both the table and the curves show clearly that the widths increase, as a function of  $Z$ , in the lower  $Z$  range, and then level off for intermediate and high  $Z$ . Near the lower edge of the  $Z$  range, the upper curve represents the  $^3\text{P}$  and the lower the  $^1\text{P}$  states, i.e., the  $^3\text{P}$  resonances are wider than the  $^1\text{P}$ . At the high  $Z$ , the upper curve is for  $np_{1/2}$  and the lower for  $np_{3/2}$ ;  $np_{1/2}$  states are broader than their  $p_{3/2}$  counterparts. For intermediate  $Z$ , we cannot easily characterize the

Table IV: Width ( $\Gamma$ ), effective quantum number ( $n^*$ ) and the product  $((n^*)^3\Gamma)$  for  $20p_a$  and  $20p_b$  resonances for the ions in the Ne isoelectronic sequence.

Z	$n^*(20p_a)$	$n^*(20p_b)$	$\Gamma(20p_a)$	$\Gamma(20p_b)$	$(n^*(20p_a))^3$	$(n^*(20p_b))^3$
			$\times 10^{(-4)} \text{ (eV)}$	$\times 10^{(-4)} \text{ (eV)}$	$\times \Gamma(20p_a)$	$\times \Gamma(20p_b)$
10	19.12034	19.17585	0.760	0.315	0.531252	0.222113
11	19.31165	19.34998	1.222	0.533	0.880095	0.386161
12	19.43293	19.45852	1.65	0.802	1.210874	0.590886
13	19.51473	19.53571	2.085	1.109	1.549508	0.826836
14	19.57532	19.59233	2.45	1.39	1.837777	1.045377
15	19.62166	19.63592	3.17	1.65	2.394785	1.249216
18	19.71376	19.72323	5.365	2.8	4.110344	2.148286
19	19.73477	19.74353	6.01	3.195	4.619242	2.458925
20	19.75263	19.76093	6.89	3.46	5.309994	2.669920
23	19.79384	19.80116	8.9	4.54	6.902083	3.524745
24	19.80451	19.81166	9.6	5.1	7.456990	3.965818
26	19.82263	19.82955	10.3	5.7	8.022709	4.444403
28	19.83746	19.84431	10.8	6.2	8.431055	4.845066
32	19.86009	19.86726	11.7	7.2	9.164937	5.646072
36	19.87651	19.88423	11.9	7.8	9.344743	6.132265
40	19.88884	19.89724	12.4	8.4	9.755512	6.616949
48	19.90587	19.91596	12.9	8.7	10.174971	6.872630
54	19.91428	19.92586	13	8.9	10.266849	7.041112
60	19.92037	19.93365	13	8.8	10.276271	6.970167
66	19.92466	19.93985	13	9	10.282912	7.135233
73	19.92802	19.94562	13	9	10.288115	7.141430
80	19.92977	19.95031	13	8.7	10.290825	6.908252
83	19.93003	19.95212	13	8.7	10.291228	6.910133

resonances since they are neither LS nor jj but something in between and different for each Z. The table shows that the ratio of the widths of the two resonances of the same n is about 2.5 at low Z, and this drops to about 1.5 at high Z.

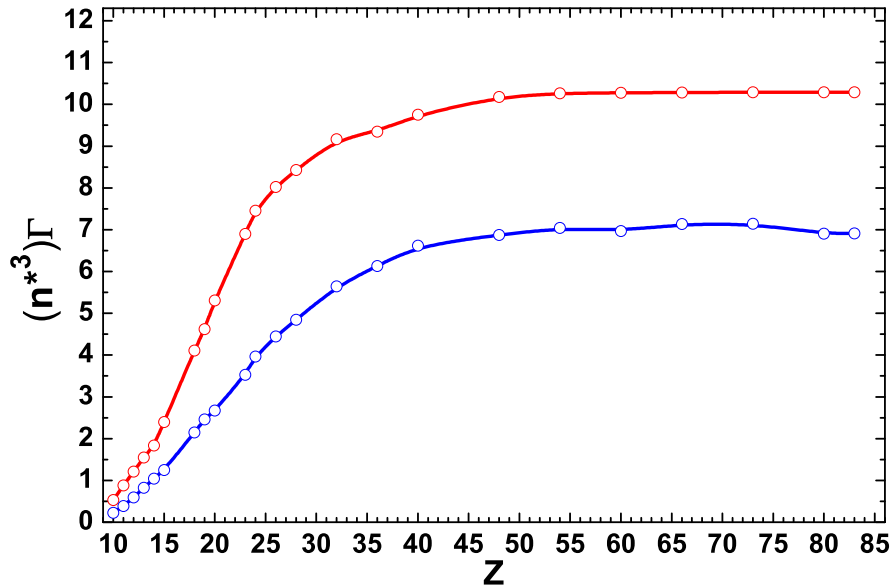


Figure 11: Behaviour of  $(n^*)^3\Gamma$  for the  $20p_a$  (upper curve) and  $20p_b$  (lower curve) resonances in Ne isoelectronic sequence.

#### IV. SUMMARY AND CONCLUSIONS

The  $2s \rightarrow np$  resonances for a number of members of the Ne isoelectronic sequence have been investigated using RRPA and RMQDT. Asymptotic quantum defects and widths were obtained for a number of members of the sequence and the results presented and analyzed. Since these quantities behave smoothly, as a function of  $Z$ , the data for any member of the sequence not calculated directly can be obtained by interpolation. For each  $Z$ , there are two series of  $2s \rightarrow np$  transitions, which lead to  $1s^2 2s 2p^6 np$   $J=1$  resonances, that are distinguished by two different angular momentum couplings. At low  $Z$ , these  $1s^2 2s 2p^6 np$   $J=1$  resonances can be characterized as  $^1P_1$  (optically allowed) and  $^3P_1$  (optically forbidden); it was seen that the transition to the optically allowed resonance state was much stronger at low  $Z$ , as expected. At high  $Z$ , the coupling is  $jj$  and the resonance states are characterized as  $[\{1s^2 2s 2p^6\}_{1/2} np_{1/2}]$   $J=1$ , and  $[\{1s^2 2s 2p^6\}_{1/2} np_{3/2}]$   $J=1$ ;  $jj$  coupling is reached by approximately  $Z=40$ . At intermediate  $Z$ , the coupling differs at each  $Z$  as we pass from LS to  $jj$  coupling, with increasing  $Z$ . Good agreement was found with experiment and previous theory generally, although certain discrepancies were noted, for e.g., with a previous calculation of the quantum defect of these resonances for  $\text{Cu}^{19+}$  [54]. Since the quantum defects, along this isoelectronic series are monotone decreasing, the comparison showed clearly that

the results of the earlier calculation were inaccurate since their values were larger than even  $\text{Ar}^{8+}$  where the values were confirmed by experiment; this shows the utility of performing calculations of an isoelectronic sequences which allow the results for individual  $Z$  to be in perspective.

Finally, it was demonstrated that, to get an accurate characterization of a resonance, a rather fine energy mesh must be used. Results were shown at three different energy meshes which gave rather different pictures of the  $2s \rightarrow 5p$  resonance in  $\text{Ar}^{8+}$ .

## ACKNOWLEDGMENTS

This work was supported in part by the Government of India, Department of Science and Technology, NSF and the US Department of Energy, Office of Chemical Sciences.

- 
- [1] B. Rudek et al., *Nat. Phot.* **6**, 858 (2012).
  - [2] W.-C. Chu, and C. D. Lin, *Phys. Rev. A* **85**, 013409 (2012).
  - [3] H. S. Chakraborty, P. C. Deshmukh, E. W. B. Dias, and S. T. Manson, *Astrophys. J.* **537**, 1094 (2000).
  - [4] A. Neogi, E. T. Kennedy, J.-P. Mosnier, P. van Kampen, J. T. Costello, G. O'Sullivan, M. W. D. Mansfield, Ph. V. Demekhin, B. M. Lagutin, and V. L. Sukhorukov, *Phys. Rev. A* **67**, 042707 (2003).
  - [5] H. Beutler, *Z. Phys.* **93**, 177 (1935); U. Fano, *Nuovo Cimento* **12**, 156 (1935).
  - [6] U. Fano, *Phys. Rev.* **124**, 1866 (1961).
  - [7] U. Fano and J. W. Cooper, *Rev. Mod. Phys.* **40**, 441 (1968).
  - [8] S. B. Whitfield, R. Wehlitz, H. R. Varma, T. Banerjee, P. C. Deshmukh, and S. T. Manson, *J. Phys. B* **39**, L335 (2006).
  - [9] V. Radojević, and J. D. Talman, *J. Phys. B* **23**, 2241 (1990).
  - [10] J. Ganz, M. Raab, H. Hotop, and J. Geiger, *Phys. Rev. Lett.* **53**, 1547 (1984).
  - [11] S. O. Kastner, A. M. Crooker, W. E. Behring, and L. Cohen, *Phys. Rev. A* **16**, 577 (1977).
  - [12] W. R. Johnson, and M. Le Dournef, *J. Phys. B* **13**, L13 (1980).
  - [13] I. D. Petrov, V. L. Sukhorukov, T. Peters, O. Zehnder, H. J. Wörner, F. Merkt, and H. Hotop,

- J. Phys. B **39**, 3159 (2006).
- [14] L. Journel, B. Rouvellou, D. Cubaynes, J. M. Bizau, F. J. Wuilleumier, M. Richter, P. Sladeczek, K.-H. Selbmann, P. Zimmermann, and Bergeron H, Jour. Phys. IV **3**, 217 (1993).
- [15] C. D. Caldwell, and M. O. Krause, J. Phys. B **23**, 2233 (1990).
- [16] K. Codling, R. P. Madden, and D. L. Ederer, Phys. Rev. **155**, 26 (1967).
- [17] C. M. Teodorescu, J. M. Esteva, R. C. Karnatak, A. El Afif, and M. Womes, J. Phys. B **30**, 4293 (1997).
- [18] K. Radler, and J. Berkowitz, J. Chem. Phys. **70**, 216 (1979).
- [19] K. Schulz, M. Domke, R. Püttner, A. Gutiérrez, G. Kaindl, G. Miecznik, and C. H. Greene, Phys. Rev. A **54**, 3095 (1996).
- [20] T. Osawa, Y. Tohyama, S. Obara, T. Nagata, Y. Azuma, and F. Koike, J. Phys. B **41**, 245206 (2008).
- [21] H. S. Chakraborty, A. Gray, J. T. Costello, P. C. Deshmukh, G. N. Haque, E. T. Kennedy, S. T. Manson, and J.-P. Mosnier, Phys. Rev. Lett. **83**, 2151 (1999).
- [22] J.-M. Bizau, J.-P. Mosnier, E. T. Kennedy, D. Cubaynes, F. J. Wuilleumier, C. Blancard, J.-P. Champeaux, and F. Folkmann, Phys. Rev. A **79**, 033407 (2009).
- [23] M. C. Simon et al., J. Phys. B **43**, 065003 (2010); and private communication.
- [24] J.-P. Mosnier et al., Phys. Rev. A **68**, 052712 (2003).
- [25] L. Liang, Z. Chao, and Z.-X. Xie, Opt. Commun. **282**, 558 (2009).
- [26] J. George, G. B. Pradhan, M. Rundhe, J. Jose, G. Aravind, and P. C. Deshmukh, Can. J. Phys. **90**, 547 (2012).
- [27] J. B. West, T. Andersen, R. L. Brooks, F. Folkmann, H. Kjeldsen, and H. Knudsen, Phys. Rev. A **63**, 052719 (2001).
- [28] V. L. Sukhorukov, I. D. Petrov, M. Schäfer, F. Merkt, M.-W. Ruf and H Hotop, J. Phys. B **45**, 092001 (2012).
- [29] L. C. Gao, D. H. Zhang, L. Y. Xie, J. G. Wang, Y. L. Shi, and C. Z. Dong, J. Phys. B **46**, 175402 (2013).
- [30] M.C. Witthoef, M.A. Bautista, J. García, T.R. Kallman, C. Mendoza, P. Palmeri, and P. Quinet, Atomic Data and Nuclear Data Tables **99**, 53 (2013).
- [31] A.K.S. Jha, P. Jha, S. Tyagi, and M. Mohan, Eur. Phys. J. D **39**, 391 (2006).
- [32] W. R. Johnson, C. D. Lin, K. T. Cheng, and C. M. Lee, Phys. Scr. **21**, 409 (1980).

- [33] C. M. Lee, and W. R. Johnson, *Phys. Rev. A* **22**, 979 (1980).
- [34] M. J. Seaton, *Proc. Phys. Soc.* **88**, 801 (1966).
- [35] M. J. Seaton, *Rep. Prog. Phys.* **46**, 167 (1983).
- [36] R. L. Kelly, *J. Phys. Chem. Ref. Data* **16**, Suppl. 1 (1987).
- [37] W. Persson, *Phys. Scr.* **3**, 133 (1971).
- [38] W. C. Martin, and R. Zalubas, *J. Phys. Chem. Ref. Data* **10**, 1 (1981).
- [39] A. E. Kramida, Yu. Ralchenko, and J. Reader, and NIST ASD Team (2014). NIST Atomic Spectra Database (ver. 5.2), [Online]. Available: <http://physics.nist.gov/asd>[2014, November 13]. National Institute of Standards and Technology, Gaithersburg, MD.
- [40] W. L. Wiese, J. R. Fuhr, and T. M. Deters, *J. Phys. Chem. Ref. Data* **7**, 267 (1996).
- [41] J. A. R. Samson, and W. C. Stolte, *J. Electron Spectrosc. Relat. Phenom.* **123**, 265 (2002).
- [42] D. Hochstuhl, and M. Bonitz, *J. Phys. Conf. Ser.* **427**, 012007 (2007).
- [43] P. G. Burke, and K. T. Taylor, *J. Phys. B* **8**, 2620 (1975).
- [44] J. M. Bizau, and F. Wuilleumier, *J. Electron Spectrosc. Relat. Phenom.* **71**, 205 (1995).
- [45] W. F. Chan, G. Cooper, X. Guo, and C. E. Brion, *Phys. Rev. A* **45**, 1420 (1992).
- [46] L. Liang, Y. C. Wang, and Z. Chao, *Phys. Lett. A* **360**, 599 (2007).
- [47] J. M. Esteva, and G. Mehlman, *Astrophys. J.* **193**, 747 (1974).
- [48] N. Singh, and M. Mohan, *Pramana* **58**, 639 (2002).
- [49] L. Liang, S.-K. He, and Z. Chao, *J. Quant. Spec. Rad. Trans* **111**, 2460 (2010).
- [50] J. Cooper, and R. N. Zare, *J. Chem. Phys.* **48**, 942 (1968).
- [51] S. T. Manson, *J. Electron Spectrosc.* **1**, 413 (1972).
- [52] S. T. Manson, and A. F. Starace, *Rev. Mod. Phys.* **54**, 389 (1982).
- [53] W. R. Johnson, and K. T. Cheng, *J. Phys. B* **12**, 863 (1979).
- [54] Z.-R. Zhang, X.-L. Cheng, Z.-J. Liu, J.-H. Yang, and H.-F. Li, *Chin. Phys. B* **21**, 013101 (2012).
- [55] B. Langer, N. Berrah, R. Wehlitz, T. W. Gorczyca, J. Bozek, and A. Farhat, *J. Phys. B* **30**, 593 (1997).
- [56] M. Stener, P. Decleva, and A. Lisini, *J. Phys. B* **28**, 4973 (1995).
- [57] E. Heinrich-Josties, S. Pabst, and R. Santra, *Phys. Rev. A* **89**, 043415 (2014).
- [58] T. B. Lucatorto, and T. J. McIlrath, *Phys. Rev. Lett.* **37**, 428 (1976).
- [59] W. Cunto, C. Mendoza, F. Ochsenbein, and C. J. Zeippen, *Astron. Astrophys.* **275**, L5 (1993).

